Emission linewidth broadening in quantum cascade lasers induced by multiple intersubband transitions

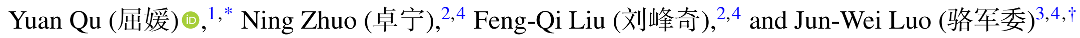

Yuan Qu (屈媛), [1,*] Ning Zhuo (卓宁), [2,4] Feng-Qi Liu (刘峰奇), [2,4] and Jun-Wei Luo (骆军委) [3,4,†]

[1] *Key Laboratory of Semiconductor Photovoltaic Technology at Universities of Inner Mongolia Autonomous Region, Inner Mongolia University, Hohhot 010021, China*

[2] *Key Laboratory of Semiconductor Materials Science, Institute of Semiconductors, Chinese Academy of Sciences, Beijing 100083, China*

[3] *State Key Laboratory of Superlattices and Microstructures, Institute of Semiconductors, Chinese Academy of Sciences, Beijing 100083, China*

[4] *Center of Materials Science and Optoelectronics Engineering, University of Chinese Academy of Sciences, Beijing 100049, China*

(Received 14 February 2024; revised 3 May 2024; accepted 6 June 2024; published 21 June 2024)

Extensive efforts are being made to improve the material quality of semiconductor quantum cascade lasers (QCLs) to suppress the carrier scattering from the interface roughness (IFR), which is commonly regarded as the leading cause of the emission linewidth broadening in QCLs. Here, we uncover an intrinsic lower bound to the emission linewidth in the prevailing QCLs by performing atomistic pseudopotential calculations of the electronic and optical properties without *ad hoc* assumptions as made in standard effective mass approaches. We demonstrate that our atomistic simulation results could reproduce the experimental results well on both emission peaks and emission linewidths for a wide range of temperatures and applied bias voltages, even without considering the effect of the IFR. Specifically, we find that the multiple intersubband optical transitions, which are broadened each by the nonparabolicity of subband energy dispersions, render a very broad emission spectrum and could explain the experimentally measured spectra for a wide external bias. Therefore, we illustrate that the previously ignored multiple intersubband optical transitions give rise to an intrinsic lower bound to the emission linewidth in QCLs. These findings imply that the IFR may play a minor role in broadening the emission linewidth in the state-of-the-art QCLs and shed light on the design of QCLs.

DOI: 10.1103/PhysRevB.109.235304

I. INTRODUCTION

Quantum cascade lasers (QCLs) are unipolar semiconductor lasers and rely on the electronic transitions of only one type of carrier between distinct subbands arising from one parent bulk conduction or valence band due to size quantization in semiconductor heterostructures [1,2]. The energy spacing of the lasing subbands determines the radiation frequency of QCLs. It thus enables tailoring the lasing emission wavelength by tuning the size in confined dimensions using the same heterostructure material to cover a wide spectral range from the midinfrared to the submillimeter wave region (∼100 μm) of the electromagnetic spectrum [2], a portion of the spectrum not easily accessible with conventional semiconductors lasers in which the band gap of the active material determines the emission wavelength [3]. For instance, the QCL has long been the preferred choice in many attempts to fabricate terahertz semiconductor lasers to bridge the so-called terahertz gap in the electromagnetic spectrum between the realms of semiconductor electronic and photonic sources [4]. Since the demonstration at Bell Laboratories by Faist *et al.* [1], QCLs have undergone tremendous advances in output power, wall plug efficiency (WPE), beam quality, and wavelength coverage and tenability [5,6]. QCLs have now become the leading laser sources with lasing wavelengths from 3 to 300 μm [7,8] covering the midinfrared and far-infrared regions. Specifically, the midinfrared QCLs have achieved a continuous-wave output power of up to 5.1 W with 21% WPE at room temperature [9], whereas the far-infrared QCLs can only achieve watt-level power at a cryogenic temperature [10,11]. The recently recorded working temperature of terahertz QCLs is 250 K [12]. Therefore, operations far below room temperature prevent far-infrared or terahertz QCLs from extensive applications [13,14].

In addition to operation at long wavelengths, QCLs have another compelling feature of a narrow linewidth of the laser transition and corresponding large optical gain regarding the peak gain cross-section g_c (or the maximum gain at resonance), which is inversely proportional to the emission linewidth γ and wavelength λ [3]: $g_c \sim 1/(\lambda \times \gamma)$. In conventional semiconductor lasers, because photons are generated by the radiative recombination of electrons in the conduction band with holes in the valence band across the band gap of the active material, the population inversion broadly distributed between these two bands having dispersion with opposite curvature results in a relatively broad gain spectrum [15]. However, in QCLs, because the lasing arises from the electronic transitions between conduction subbands having a nearly parallel curvation with a negligible nonparabolicity, the population inversion created between these subbands results in a narrow gain spectrum that is expected to be like a δ function in the absence of collision-induced broadening [1,2,15]. This narrow gain spectrum will be much less sensitive to the thermal broadening of the electron distribution,

*Contact author: quyuan@imu.edu.cn
†Contact author: jwluo@semi.ac.cn

 ©2024 American Physical Society

unlike the gain spectrum associated with interband transitions in conventional semiconductor lasers [1]. Furthermore, the gain of the active material becomes more sensitive to the emission linewidth in a longer wavelength laser, which may be responsible for the fact that, to date, the QCLs that operate in the terahertz region have been limited to low temperatures that necessitate cryogenic cooling [16]. Indeed, it was recognized that, as the temperature rises, a reduced peak gain cross-section g_c with elevated threshold current could directly cause a drop in WPE and out power and even failure in QCLs [17].

In reality, the optical emissions in QCLs were found experimentally to have a finite linewidth, which becomes wider at a higher temperature [18]. The broadening to the emission linewidth is regarded entirely as arising from the collisional dephasing of electrons in the upper lasing subband due to the scattering by ionized impurities, interface roughness (IFR), phonons, and other electrons [2]. Remarkably, the IFR scattering is commonly believed to be the primary mechanism responsible for the observed linewidth broadening in QCLs [19–27] since the IFR scattering-induced broadening could reproduce well the experimentally measured emission linewidth in a wide range of temperatures [22,28] by adjusting two IFR character parameters: the average roughness height Δ and correlation length Λ along the interface [29]. Much of the attention after that turns to controlling the material quality of QCL structures to suppress the IFR scattering-induced linewidth broadening to improve QCL performance [28, 30–37]. However, evidence against the IFR mechanism has been accumulated. For instance, the fitted IFR parameter Δ was considerably larger than the reported values measured directly from the QCL materials [26,33]. In SiGe QCLs, the IFR model predicted linewidth of 170–330 meV [22] is a factor of 4–5 larger than the experimentally measured value of 40 meV [38], and thus, a vertical correlation length $\Lambda_{\perp}$ has been introduced additionally to the IFR scattering model to cure the overestimation [22,33]. Because the IFR scattering is not so sensitive to temperature, the scattering by optical phonons has been added to explain the broader linewidths observed at higher temperatures [20]. Very recently, Kolek *et al.* [26] also found that the IFR scattering contributes only 50% of the optical emission linewidth by considering the k dependence of the upper lasing subband states due to the finite carrier concentration. Furthermore, the linewidth broadening induced by optical transitions from the upper lasing subband to multiple lower subbands spanning an energy range of 20 meV has also been predicted theoretically in a bound-to-continuum design of terahertz QCLs [21] but was overlooked due to its overlap with a wider linewidth of 15–25 meV predicted from the IFR scattering model [39]. Recently, Bosco *et al.* [40] followed by Khalatpour *et al.* [12] achieved temperature leaps of 10 and 40 K, respectively, to a maximum operating temperature of 250 K for terahertz QCLs by replacing the prevailing bound-to-continuum design with a two-well design in a dramatic sacrifice of the extraction efficiency. Although such improvement was attributed to the overcoming of the band misalignment caused by higher doping levels in the previous design and being insensitive to dephasing caused by IFR and impurities [12], the reduced linewidth by changing the multiple intersubband transitions to single intersubband transitions may also play an essential role. Franckié *et al.* [41] found that the temperature degradation of the two-well design is dominated by level broadening. These pieces of evidence indicate that we must revisit the mechanisms underlying the linewidth broadening in QCLs.

In this paper, we examine explicitly the effect of multiple intersubband transitions and nonparabolicity in conduction subbands on the emission linewidth of QCLs by performing full-zone and multiband electronic structure calculations using a sophisticated atomistic pseudopotential method without *ad hoc* assumptions [42–44]. We demonstrate that our theoretical results reproduce the experimental emission peak well for a wide range of temperatures and applied bias voltages even without considering the IFR. We show that the previously ignored multiple intersubband transitions, which are each broadened by the nonparabolicity of subband dispersion, remarkably modify the emission spectrum and give rise to a lower bound to the emission linewidth in prevailing bound-to-continuum or double-phonon resonance designs of QCLs. These findings shed light on understanding the intrinsic broadening and reveal design principles of QCLs.

II. ATOMISTIC SIMULATION METHOD

The classical $\mathbf{k}\cdot\mathbf{p}$ theory is a standard method for band structure design of semiconductor QCLs. One can learn from the $\mathbf{k}\cdot\mathbf{p}$ approximation that the nonparabolicity of the energy bands in bulk semiconductors is entirely attributed to the coupling to other bands with their coupling strengths characterized by dipole matrix elements [45]. If the $\mathbf{k}\cdot\mathbf{p}$ Hamiltonian is diagonalized by using a sufficiently large number of Bloch states of bulk bands at $\mathbf{k}_0$, it would correctly predict the full (nonparabolic) band dispersion throughout the Brillouin zone. However, the number of required $\mathbf{k}\cdot\mathbf{p}$ parameters increases rapidly with the number of included bulk bands and thus renders it a difficult-to-compute task [46,47]. Traditionally, the set of Bloch states is truncated to those bulk bands strongly coupled by the $\mathbf{k}\cdot\mathbf{p}$ perturbation, namely, those near the band gap. For a III-V zinc-blende semiconductor, the three p-derived Bloch states of the valence bands, which are degenerate at the Γ point, are usually augmented by the Bloch state of the first conduction band to give rise to the 8×8 $\mathbf{k}\cdot\mathbf{p}$ (including spin degeneracy). For the energy dispersion of the conduction band in the proximity of the Γ point, a nondegenerate perturbation theory could further reduce the eight-band $\mathbf{k}\cdot\mathbf{p}$ model to a one-band effective mass model by treating its coupling with three valence bands as second-order perturbation. Thus, the energy band is approximated to be parabolic ($\sim k^2$) around their extreme [48–50] with a correction (depending on $\sim k^4$) due to the nonparabolicity of the band [2]:

$$E(k) = \frac{\hbar^2 k^2}{2m_c^*}(1-\gamma k^2), \tag{1}$$

where

$$\gamma = \frac{\hbar^2}{2m_c^* E_g} \tag{2}$$

is the nonparabolicity coefficient, m_c^* is the effective mass of the lowest conduction band at the Γ point ($k=0$), and E_g is

the band gap. In general, the resolution of the expansion is limited since the basis set is restricted.

These limitations of the $\mathbf{k}\cdot\mathbf{p}$ approximation could be circumvented by solving the Schrödinger equation in an atomistic method. For instance, the atomistic tight-binding method [51] has been used to study the band structure of QCLs [52]. In this paper, we instead use an atomistic computational approach based on a semiempirical pseudopotential method (SEPM) for semiconductors. In the atomistic SEPM method, crystal (or nanostructure) potential $V(\mathbf{r})$ is obtained by the sum of atomistic potentials and eigensolutions expanded within a complete basis set of a sufficiently large number of plane waves [53–56]. The Schrödinger equation governing the motion of an electron in a QCL with an atomistic pseudopotential crystal potential $V(\mathbf{r})$ [42] is

$$\hat{H}\psi_i(\mathbf{r}) = \left[\frac{\hat{p}^2}{2m} + V(\mathbf{r})\right]\psi_i(\mathbf{r}) = \varepsilon_i\psi_i(\mathbf{r}), \tag{3}$$

where $V(\mathbf{r}) = \sum_n \sum_\alpha v_\alpha(\mathbf{r} - \mathbf{R}_n - \mathbf{d}_\alpha)$ is a superposition of screened atomic potentials v_α of atom type α at site $\mathbf{d}_\alpha$ in the nth primary cell $\mathbf{R}_n$. The indices (α, n) extend over the QCL and the barrier materials. The equilibrium position of each atom in the supercell of the QCL is obtained by minimizing the lattice-mismatch-induced strain energy in terms of the atomistic valence force field [57]. The atomic pseudopotentials v_α were empirically fit to experimental transition energies, effective masses, spin-orbit splitting, deformation potentials of the underlying bulk semiconductors, and band offsets of two different semiconductors associated with a heterojunction (c.f. Refs. [58,59] for details). In contrast with the first-principles methods based on density functional theory (DFT), which had been widely used to calculate the electronic structure of small systems, the overestimation of effective masses (∼40%) and underestimation of band gap (∼60%) are corrected in the current atomistic screened pseudopotential method by fitting them to experimental values [60]. The Schrödinger equation of Eq. (1) is solved by expanding the electronic states $\psi_i(\mathbf{r})$ of one stage of QCLs in a plane-wave basis set and selectively calculating the band-edge states using the folded-spectrum method [61]. This approach naturally captures the atomistic symmetry of the system, multiband, intervalley, and spin-orbit interactions. It thus could reproduce the nonparabolic band dispersion throughout the whole Brillouin zone. The computation capacity of our atomistic method is aggressively extended from <1000 atoms of DFT (and <100 atoms using the GW and Bethe-Salpeter method) to up to millions of atoms with the present method [61], provided that we restrict our attention to a fixed energy window around the fundamental band gap.

The validity of the empirical pseudopotential method (EPM) and modified SEPM developed in Zunger's group [42] has been well established in the past seven decades. A direct comparision beween SEPM calculation of band structure in GaAs/AlAs superlattices and quantum wells (QWs) with the results using the eight-band $\mathbf{k}\cdot\mathbf{p}$ approach shows [45] that there are systematic errors in band energies and dispersion for deeper hole subbands (all other than the heavy- and light-hole first subbands hh1 and lh1) and significant qualitative and quantitative errors for the conduction subbands. We have extensively utilized the SEPM to calculate electronic and optical properties and directly compare them with experimental data for semiconductor superstructures [54], including superlattices, and QWs [53,56,62–64], quantum dots [65–67], and quantum wires [55,68]. In these works, we have demonstrated that our atomistic pseudopotential method can accurately capture the energy separation between single-particle energy levels and many-body excitonic levels. For instance, we can reproduce the fine structure splitting of excitons in an energy scale as low as μeV [66,67] by fitting precisely to the band structure of their parent bulk InAs and GaAs with <10 meV deviations from the experimental band gap and <2% difference from the experimental electron effective mass [58].

III. RESULTS AND DISCUSSION

QCLs with two-phonon resonance [39,69] and bound-to-continuum [17,39,70] active region designs have been demonstrated to have much better performance than the traditional three-level designs, resulting from an effective extraction of electrons from the lower lasing subband offered by a ladder of subbands separated by an optical phonon [39]. These two designs have now become prevailing QCL designs [71,72]. Here, we theoretically examine the optical transitions and intrinsic emission linewidth of a well-studied two-phonon resonance $Al_{0.48}In_{0.52}As/Ga_{0.47}In_{0.53}As$ QCL by neglecting the collision-induced broadening caused by the IFR, impurity, and phonons [21]. This QCL design is experimentally measured to have an emission wavelength of $\lambda = 8.4$ μm (or photon energy 148 meV) at the threshold bias voltage of 8 V [21]. Figure 1(a) schematically shows the energy band diagram for one stage of this QCL, which consists of an active region made by four QWs and a collector region (or an injector of the following stage) made by eight QWs under the threshold bias voltage. These two regions are separated by a so-called $Al_{0.53}In_{0.47}As$ extraction barrier layer, with its thickness alone used to distinguish the two-phonon design (2.2 nm thick) from the bound-to-continuum design (1.2 nm thick) [21]. Therefore, these two QCL designs have 12 QWs per stage. Note that, to schematically diagram the band alignment of the QCL in Fig. 1(a), we artificially use sharp well/barrier interfaces for simplicity. Although we deal with ideal interfaces by neglecting the IFR along the in-plane direction, the atomic strain and atom random distributions of alloy barriers modify the local band structure at interfaces [57], leading to an asymptotic potential in the interface plane rather than a flat one [58], since the atomic strain and atom random distributions of alloy barriers modify the local band structure at interfaces [57].

Figure 1(a) also shows the squared modulus of the wave functions of the subband edge-states at $\mathbf{k}_{||} = 0$ in the two-dimensional (2D) Brillouin zone for one stage of the two-phonon resonance design. There are 13 bound states numbered in ascending order in energy from $|1\rangle$ to $|13\rangle$ for the 12-quantum-well structure: each QW supplies its ground state, and the widest QW provides an additional state for the first excited subband. This excited state is numbered as $|12\rangle$ at the threshold bias voltage and is identified as the upper lasing subband. The state $|10\rangle$, which distributes mainly in

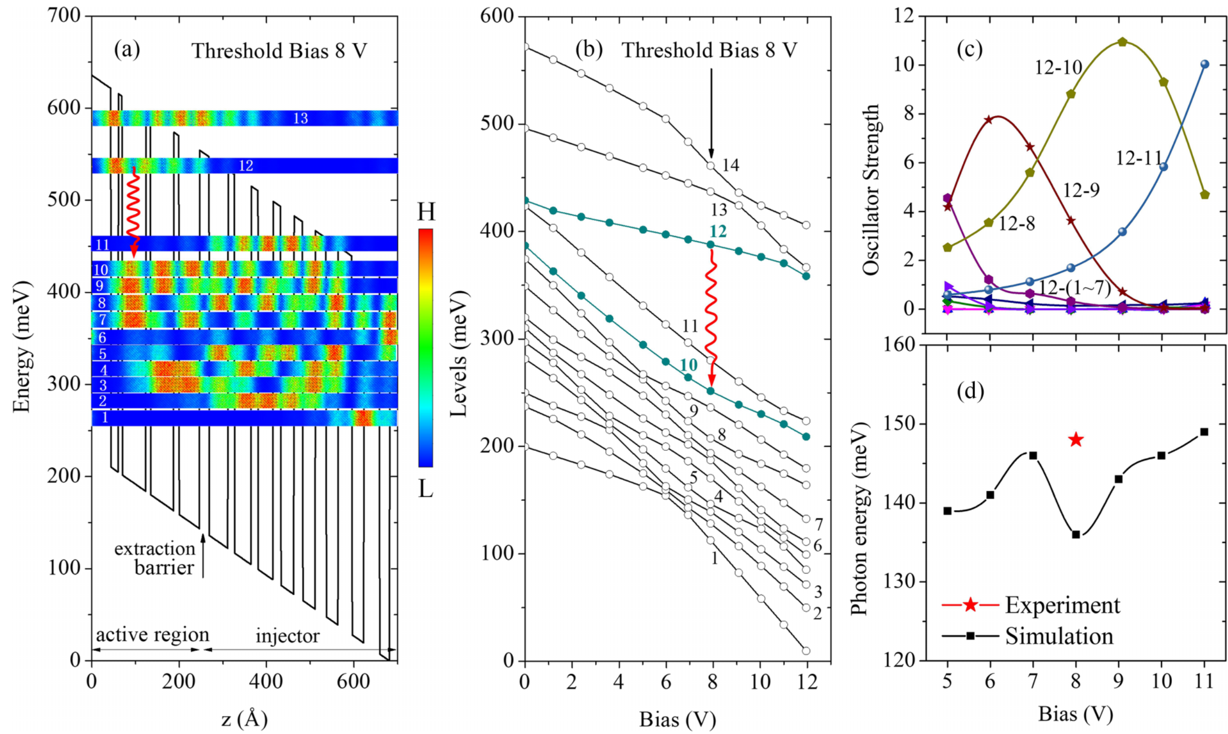

FIG. 1. The atomistic calculated band structure of a two-phonon resonance design of $Al_{0.48}In_{0.52}As/Ga_{0.47}In_{0.53}As$ quantum cascade laser (QCL) studied in Ref. [21]. (a) Squared modulus of the wave functions of subband edge-states in one stage of the QCL under the threshold bias voltage of 8 V, layer out on the bias-modified band alignment of the conduction band minimum (CBM) of the corresponding bulk materials. Each QCL stage has the layer sequence from an injector barrier to the active region as 4.3/1.7/0.9/5.4/1.1/5.3/1.2/4.7/2.2*/4.3/1.5/3.8/1.6/3.4/1.8/3.0/2.1/2.8/2.5/2.7/3.2/2.7/3.6/2.5 (numbers are the layer thickness given in nanometers), where underlined numbers are InAlAs barriers; otherwise, they are InGaAs wells. The asterisk marks the extraction barrier. (b) Subband band-edge levels as a function of bias. A vertical red arrow indicates the optical emission from the upper lasing subband $|12\rangle$ to the lower lasing subband $|10\rangle$. (c) Bias-dependent oscillator strength of the optical transition from the subband $|12\rangle$ to other low-lying subbands, (d) Theoretically predicted photon emission energy between the identified upper and lower lasing subbands as a function of gate bias voltage compared with the experimental value at the threshold bias voltage [21].

the active region and corresponds to the lower lasing subband. Such an assignment is consistent with that in Ref. [21]. The intermediate subband $|11\rangle$ between these two lasing subbands comes from the collector region, with its wave function having a vanishing overlap with that of the upper lasing subband $|12\rangle$. One can also see from Fig. 1(a) that the positive gate bias causes the bands to bend downward through the stage from the injector region to the collector region. Energy levels of subbands as a function of external gate bias varying from 0 to 11 V are shown in Fig. 1(b). The energy levels confined in wider wells have a stronger bias dependence than those confined in narrower wells. Thus, a larger gate bias gives rise to a larger band bending to switch the order of the levels. For instance, Fig. 1(b) shows that two energy levels $|10\rangle$ and $|9\rangle$ move toward each other as the gate bias rises from 5 V, at which the laser starts emitting photons, to the threshold bias of 8 V since $|10\rangle$ has a larger slop than $|9\rangle$, whereas they then move apart without crossing as the gate bias further increases. This behavior is called level anticrossing, resulting from coupling between two involved states. The amplitude of the anticrossing gap characterizes their coupling strength. Figure 1(a) shows that, at the threshold bias of 8 V, the spatial distribution of $|9\rangle$ and $|10\rangle$ states has a significant overlap, supplying the chance to have a strong coupling. It should be noted that the upper lasing subband $|12\rangle$ is well separated from others in energy as the external bias increases, which guarantees the subband $|12\rangle$ always being the upper lasing subband in the investigated gate bias, as shown in Fig. 1(b).

To confirm the identification of lasing subbands, we turn to examine the optical transitions between subbands. Figure 1(c) shows the oscillator strengths of the optical transition from the upper lasing subband $|12\rangle$ to all low-lying subbands as a function of bias. The oscillator strength of an optical transition from an initial state $|a\rangle$ to the final state $|b\rangle$ is defined as a dimensionless quantity:

$$F_{ab} = \frac{2|P_{ab}|^2}{m\hbar\omega} = \frac{2|\langle b|\mathbf{P}|a\rangle|^2}{m\hbar\omega}, \quad (4)$$

where $\mathbf{P}_{ab}$ is the momentum matrix element, and $\hbar\omega$ the energy separation between $|a\rangle$ and $|b\rangle$. One can see from Fig. 1(c) that there are multiple intersubband transitions instead of one having finite oscillator strength. Specifically, at a bias voltage of 5 V, the optical transition from the upper lasing subband $|12\rangle$ to subband $|8\rangle$ has a slightly larger oscillator strength than that from $|12\rangle$ to $|9\rangle$, and these two optical transitions have a much stronger oscillator strength than the remaining transitions. The close oscillator strengths from $|12\rangle$ to $|8\rangle$ and $|9\rangle$ are mainly due to the strong coupling

between $|8\rangle$ and $|9\rangle$ since they experience level anticrossing at $\sim$5 V, as shown in Fig. 1(b). As the gate bias increases from 5 to 6 V, the oscillator strength between $|12\rangle$ and $|9\rangle$ gets stronger, while that between $|12\rangle$ and $|8\rangle$ becomes weaker as a result of reduction in coupling between $|8\rangle$ and $|9\rangle$. At the same time, the transitions from $|12\rangle$ to $|10\rangle$ and $|11\rangle$ get stronger monotonically with increasing bias voltage up to 9 V. The oscillator strength of the transition from $|12\rangle$ to $|10\rangle$ exceeds that from $|12\rangle$ to $|9\rangle$ and becomes the strongest optical transition when the gate bias is >7 V due to level anticrossing occuring between $|9\rangle$ and $|10\rangle$, as shown in Fig. 1(b). If the strongest oscillator strength is followed, the lower lasing subband can be identified as varying from $|8\rangle$ to $|9\rangle$ and then to $|10\rangle$ with increasing the gate bias voltage, resulting from level anticrossing among them.

Once the upper and lower lasing subbands are distinguished, the energy of the emission photon vs voltage can be given, as shown in Fig. 1(d). At the experimental threshold bias voltage of 8 V, our atomistic simulation predicted emission energy of the QCL is 136 meV, close to the experimental value of 148 meV [21]. Note that emission energy exhibits abnormally strong fluctuation around the threshold bias, as shown in Fig. 1(d), due to the level anticrossing among $|10\rangle$, $|9\rangle$, and $|8\rangle$. After averaging two strong transitions, we can obtain an average emission energy of 143 meV. It is in good agreement with experimental emission energy, especially considering that our atomistic simulations do not employ any adjustable parameters and neglect the scattering from free electrons and ionized dopants on the Hartree potential.

After the optical transition from the upper lasing subband to the lower lasing subband, a swift extraction of electrons from the lower lasing subband is another critical process in the operation of QCLs to achieve population inversion. The optical phonons could effectively assist the extraction thanks to the ultrafast scattering of electrons between two subbands in a picosecond time scale when their energy separation approaches the optical phonons. The ultrafast carrier extraction process is three orders of magnitude faster than the optical radiation process (in ns) and thus could effectively achieve population inversion. The condition for lasing is the optical gain can compensate for the loss. The key to such band design lies in spacing the lower lasing level and extraction level to the energy of an optical phonon [2]. However, it is challenging to maintain such an accurate energy level spacing when the actual QCL operates under external voltage. Thus, a double-phonon resonance extraction structure or a bound-to-continuum structure is proposed to ensure the extraction efficiency of electrons following the optical transition [39,73]. Our atomistic simulations show that, under the threshold bias 8 V, the energy separation from level $|10\rangle$ to level $|8\rangle$ is 45 meV, and that from level $|8\rangle$ to level $|5\rangle$ is 37 meV, which are very close to the energies of the longitudinal optical (LO) phonons of the $Al_{0.48}In_{0.52}As$ barrier (46 meV) and $Ga_{0.47}In_{0.53}As$ well (34 meV) alloys [74,75], respectively. A ladder of three states separated in energy by an optical phonon in the two-phonon resonance design enables a fast electron extraction by emission of two optical phonons to the $Al_{0.48}In_{0.52}As$ barrier and $Ga_{0.47}In_{0.53}As$ well as designed [21], respectively. We can safely conclude that our atomistic simulations reproduce the two-phonon design of the QCL well without having adjustable parameters. This agreement is even better considering the spectrum broadening by multiple intersubband transitions.

According to what we have discussed above and shown in Fig. 1(c), the introduction of additional energy levels in the collector region to improve the extraction efficiency will have a side effect in that the electrons in the upper lasing subband will have a certain probability to transition to these extraction levels, which will inevitably broaden the gain spectrum. Figures 2(a)–2(c) show the oscillator strengths against the transition energy for all transitions from the upper lasing level $|12\rangle$ to lower-lying levels compared with the experimental emission spectrum [21] for the QCL under external bias voltages of 6, 8, and 10 V, respectively. To account for the slight underestimation of the QCL emission energy mentioned above, the experimental emission spectra [21] are redshifted by 14–17 meV to align the theoretical spectra obtained from our atomistic simulations. Interestingly, we can lay out the experimental emission spectrum measured at room temperature [21] to have a high overlap with our theoretically predicted oscillator strength spectrum for each external bias voltage. Note that we neglect the IFR scattering-induced linewidth broadening in our atomistic simulation. Specifically, Fig. 2(a) shows that four optical transitions from $|12\rangle$ to $|8\rangle$–$|11\rangle$ exhibit significant oscillator strengths at the bias voltage of 6 V with an energy spanning $\sim$80 meV. Raising the bias voltage to 8 V, three optical transitions from the upper lasing level $|12\rangle$ to $|9\rangle$, $|10\rangle$, and $|11\rangle$ levels stand out clearly with the remaining oscillators being extremely weak. The transition from $|12\rangle$ to $|10\rangle$ has a much stronger oscillator than that from $|12\rangle$ to $|9\rangle$ and $|11\rangle$, giving rise to a spectrum spanning $\sim$50 meV. Further raising the bias voltage to 10 V, the oscillator strength mainly concentrates on two optical transitions from $|12\rangle$ to $|11\rangle$ and $|10\rangle$ with the energy span further narrowed to $\sim$12 meV. It demonstrates that the emission linewidth narrowing vs bias voltage could be entirely explained by the energy span of the multiple intersubband transitions. On closer inspection of the change of the wave functions with bias voltage, we found that the decoupling of the electronic states in the collector region by the tilted conduction band suppresses the multiple intersubband transitions. We also notice that the effect of finite oscillator strengths of the upper lasing subband to multiple lower subbands on the spectrum broadening has been mentioned in a bound-to-continuum design of terahertz QCLs [21], the impact of which on QCL performance was overlooked due to an assumed wider linewidth of 15–25 meV induced by the IFR scattering.

Each intersubband transition can be broadened by the collisional dephasing of electrons in the upper lasing subband due to the scattering by ionized impurities, IFR, phonons, and other electrons [2] as well as the nonparabolicity of subbands, which has been regarded as negligible. Here, we examine the effect of the nonparabolicity of the lasing subbands on broadening the emission linewidth by neglecting the collisional dephasing factors. In the context of QCLs, the one-band effective mass approximation models [21,76] are exclusively employed to describe the electronic structure, in which an energy-dependent mass is used to correct the energy levels of subbands. However, the deviation from the parabolic energy dispersion gives rise to nonparabolicity, which

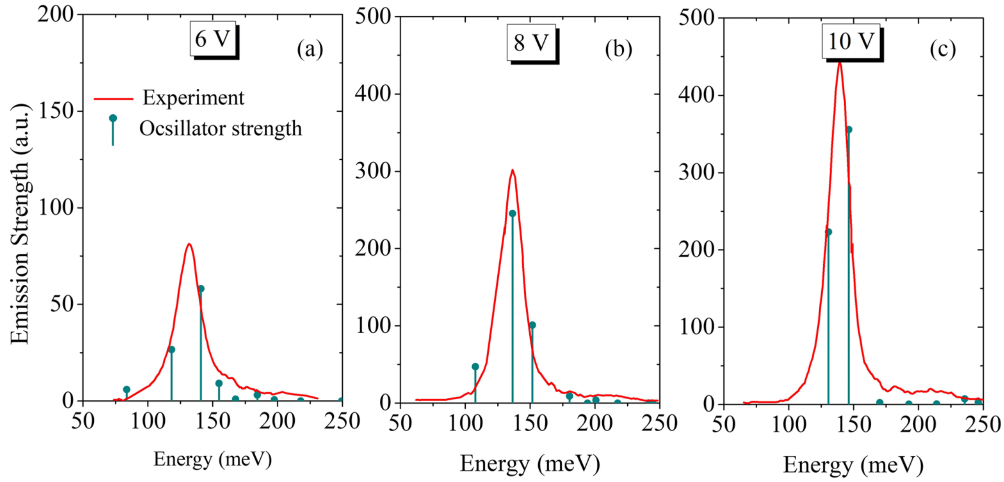

FIG. 2. Oscillator strengths of the optical transitions from the upper lasing level |12⟩ to all lower-lying levels |1⟩–|11⟩ in comparison with the experimentally measured emission spectrum [21] for a double-phonon resonance design under external biases of (a) 6 V, (b) 8 V, and (c) 10 V. To have a better alignment, we redshift the experimental spectrum by 14–17 meV, which is responsible for the slight underestimation of the quantum cascade laser (QCL) emission energy by our atomistic simulation.

occurs even in the simplest band of the lowest conduction band of semiconductors near the Γ point. However, the nonparabolicity is frequently ignored in subbands, between which the electrons transition to emitting photons. Specifically, the nonparabolicity of the conduction subbands becomes essential as the in-plane wave vector gets far away from the zone center or the Γ point, resulting from high carrier concentration or high temperature. The nonparabolicity of subbands has been examined to broaden the transition as $\Delta E = E_F \frac{E_{21}}{E_G}$ according to the effective mass approximation (where E_F is the Fermi level, E_{21} the band edge separation between subbands 1 and 2, and E_G the bulk band gap of the well material). Considering the nonparabolicity of subbands, an overestimated linewidth of 20 meV was predicted in comparison with an experimentally measured linewidth of 6.6 meV [77] for an InAs/AlSb QW doped to a sheet electron density of 10^{12} cm^{-2}. It was subsequently argued [77] that the depolarization effect [78] remarkably narrows the absorption peak due to a high-density electron gas screening of the incident field. Since then, the band nonparabolicity has been completely excluded as a potential factor broadening the intersubband transitions in QCLs [2]. However, there is renewed interest in the impact of band nonparabolicity on the optical and transport properties of semiconductors [79–82] and the properties of thermoelectric materials [83,84]. We also note that Załużny [78] has demonstrated that the depolarization effect depends sensitively on the electron density and is negligible for a low density of $N_s = 1 \times 10^{11}$ cm^{-2}, which is on the order of electron densities in the upper lasing subband for operating QCLs [21,32,85,86]. By considering the nonparabolicity, authors of a very recent study illustrated that the IFR scattering contributes to only ∼50% of the optical linewidth for a QCL emitting at ∼5 μm wavelength [26]. It thus becomes necessary to accurately descibe the nonparabolicity of subbands in QCLs.

Figure 3(a) shows our atomistic-simulation-predicted nonparabolic dispersions of the lasing subbands |12⟩ and |10⟩. The upper lasing subband |12⟩ has a stronger nonparabolicity in energy dispersion than that of the lower lasing subband |10⟩, leading to a smaller emission energy of the vertical transitions as wave vector $\mathbf{k}_{||}$ moves away from the Γ point. Such nonidentical optical transition energy at different k points could broaden the emission peak of a single intersubband transition. Such broadening gets wider by lifting the temperature at which more electrons on the upper lasing subband $n_2(k_{\|})$ can be thermally excited with a large momentum wave vector, as shown in Fig. 3(b). According to Fermi's golden rule, the gain spectrum is [3]

$$g(\hbar\omega) = -\alpha(\hbar\omega), \quad (5)$$

where α is the absorption coefficient:

$$\alpha(\hbar\omega) = C_0 \frac{2}{V} \sum_{\mathbf{k}_a} \sum_{\mathbf{k}_b} |\hat{e} \cdot \mathbf{P}_{ab}|^2 \delta(E_b - E_a - \hbar\omega)(f_b - f_a), \quad (6)$$

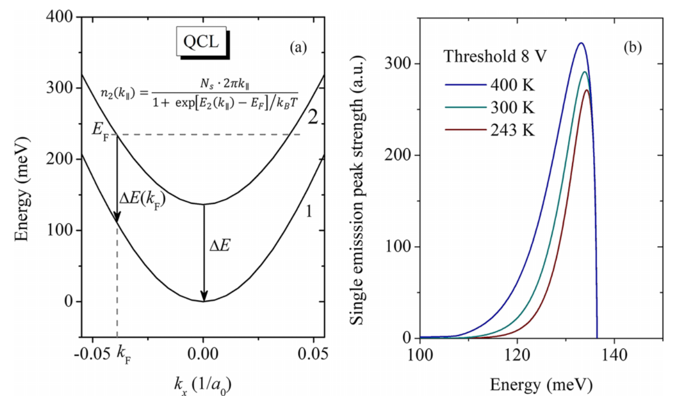

FIG. 3. (a) Atomistic pseudopotential method calculation predicted nonparabolic energy dispersions of two lasing subbands 2, 1 (here, |12⟩ and |10⟩ subbands) for a double-phonon resonance design of quantum cascade laser (QCL) given in Ref. [21]. (b) Nonparabolicity induced linewidth broadening of a single intersubband optical transition between two lasing subbands |12⟩ and |10⟩ at temperatures of 243, 300, and 400 K, respectively.

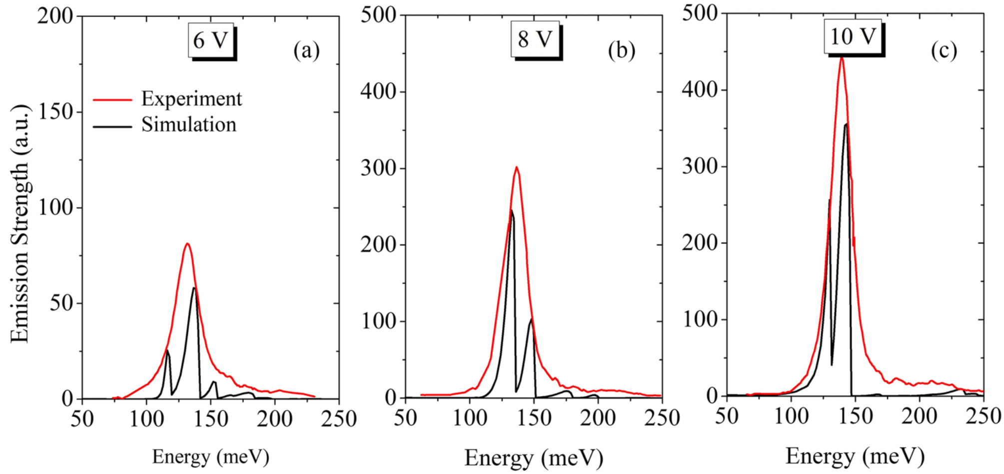

FIG. 4. Atomistic simulation predicted spectra of the two-phonon design of quantum cascade laser (QCL) at 300 K under external bias voltages of (a) 6 V, (b) 8 V, and (c) 10 V, broadened by the nonparabolicity of the subbands in comparison with the experimental spectra [21].

with coefficient $C_0 = \frac{\pi e^2}{n_r c \varepsilon_0 m_0^2 \omega}$. Here, V is the volume of the space, $\hat{e}$ is a unit vector in the direction of the optical electric field, f_b and f_a are the occupation possibilities on the initial and final levels following the Fermi-Dirac distribution, n_r is the refractive index, c is the speed of light in the free space, m_0 is the free electron mass, e is the charge of an electron, and ε_0 is the vacuum permittivity. The light emission occurs in a QCL when electrons are injected from the injector (also the collector in the preceding stage) into the upper lasing subband at a rate given by bias current. From Eq. (4), the oscillator strength F_{ab} is proportional to the square of the momentum matrix element $\mathbf{P}_{ab}$ and inversely proportional to the frequency ω. The absorption coefficient can be simplified as

$$\alpha(k_\parallel) \propto F_{ab}(n_2 - n_1). \tag{7}$$

Here, the occupation on the lower lasing subband n_1 is assumed zero considering the swift extraction. The occupation number of the upper lasing subband is weighted by

$$n_2(k_\parallel) = N_s \cdot f(k_{||}) \cdot g(k_{||}), \tag{8}$$

where $f(k_{||}) = (1 + \exp\{[E_2(k_{||}) - E_2(k_F)]/k_B T\})^{-1}$ is the Femi-Dirac distribution with Femi wave vector $k_f = \sqrt{2\pi N_s}$ determined by electron density N_s, and $g(k_{||})$ is the electron density of states (DOS) proportional to the in-plane wave vector $k_{||}$. The electron densities in the upper lasing subband in operating QCLs are usually on the order of $N_s = 1 \times 10^{11}$ cm^{-2} [21,32,85,86]. As the momentum $k_{||}$ gets away from the Γ point, the occupation number on the upper lasing subband decreases monotonically accompanied by an exponential reduction in the occupation probability according to the Fermi-Dirac distribution and a linear increase of DOS.

Figure 3(b) shows the simulated emission spectra for electron transitions from the upper lasing subband $|12\rangle$ to the lower lasing subband $|10\rangle$ at the threshold bias voltage of 8 V vs temperature. The nonparallel dispersion gives rise to the spectrum in a half-Gaussian lineshape, as shown in Fig. 3(b), rather than in the rectangular shape expected before [2]. The emission spectrum is thoroughly broadened by the nonparallel dispersion of two lasing subbands; otherwise, it is an impulse peak even without considering any scattering mechanism, as shown in Fig. 2. We must stress that the intrasubband and intersubband scatterings, which have been excluded in our simulations but exist in experiments to some extent, will smear the nonparallel dispersion-induced half-Gaussian lineshape into a full Lorentzian lineshape [2]. Rising temperature will thermally excite more electrons to higher-energy states on the upper lasing subband, broadening further the emission peak, as shown in Fig. 3(b). However, the broadening of the emission with increasing temperature observed experimentally has been completely attributed to the intrasubband and intersubband scatterings dominated by the IFR-induced scattering [21,87,88].

Figure 4 shows the theoretically predicted emission spectra, considering the broadening of each intersubband transition by the nonparabolicity of intersubbands compared with the experimentally measured emission gain spectra [21]. The impulselike isolated peaks of multiple intersubband transitions presented in the theoretically predicted oscillator spectra (shown in Fig. 2) are now remarkably broadened by nonparabolic energy dispersions of the subbands and tend to overlap each other to give rise to a single broad peak. In our atomistic simulations, we have neglected the collisional dephasing the collisional dephasing of electrons in the upper lasing subband due to the scattering by ionized impurities, phonons, other electrons, and IFR [2], which are always presented in real QCLs and will certainly further broaden the optical transitions. If we consider these broadening factors, multiple peaks of different intersubband transitions will finally emerge to a single broad with a high overlap with the experimental spectra after a slight redshift. Subsequently, we can safely conclude that the experimentally observed broad spectrum in at least two-phonon resonance and bound-to-continuum designs of QCLs is an envelope of discretely spaced multiple peaks, with each being broadened by the nonparallel dispersions of the subbands and dephasing time induced by intrasubband and intersubband scatterings.

Since the peak gain cross-section g_c is inversely proportional to the emission linewidth γ and wavelength λ [3], the

multiple intersubband-transition-induced linewidth broadening should be a critical issue to hinder the achievement of high-performance long-wavelength QCLs. This implies that the design principle for long-wavelength QCLs should try to reduce the number of subbands in the collector region (or extraction region) to narrow the emission linewidth, lower the threshold, and enhance the operation temperature. Franckié *et al.* [41] achieved a temperature enhancement of 10 K for terahertz QCLs by replacing the prevailing bound-to-continuum design with a two-well design in a dramatic sacrifice of extraction efficiency. Khalatpour *et al.* [12] further improved the performance of this two-well design to report a high-power terahertz (at ∼4 THz) QCL with a maximum operation temperature exceeding 250 K. The improvement of the operating temperature should also benefit from the significantly narrowed gain spectrum by reducing the number of subbands in the extraction region, although it was attributed to the suppression of the carrier leakage over barriers [12]. Franckié *et al.* [41] also found that the temperature degradation of the two-well design is dominated by level broadening and illustrated the enhancement in the optical gain by reducing the number of QWs in each stage of QCLs but with an argument that the carriers are more concentrated to the upper lasing subband [40].

IV. CONCLUSIONS

In this paper, we uncovered a lower bound to the linewidth broadening of the gain spectrum of the QCLs induced by multiple intersubband optical transitions and nonparabolicity of energy subbands by performing full-zone and multiband electronic structure calculations using a sophisticated atomistic pseudopotential method. Our atomistic simulations could reproduce the experimental results on both emission peaks and emission linewidths for a wide range of temperatures and applied bias voltages in the absence of IFR, which is commonly believed to be the leading factor for linewidth broadening in QCLs. Specifically, we found that the optical transitions arise from multiple pairs of subbands instead of what is commonly believed to be a single pair of subbands. These multiple intersubband optical transitions, broadened each by the nonparabolicity of subband dispersions, yield a very broad emission spectrum and could explain the experimentally measured spectra for a wide external bias even without considering the IFR. We must address that uncovered multiple intersubband transitions in QCLs and their impact on emission linewidth broadening can also be obtained from the calculation based on the eight-band $\mathbf{k}\cdot\mathbf{p}$ Hamiltonian irrespective of their accuracy. Therefore, we can draw a conclusion that the previously ignored multiple intersubband optical transitions give rise to an intrinsic lower bound to the emission linewidth in QCLs. These findings imply that the IFR may play a minor role in broadening the emission linewidth in state-of-the-art QCLs and shed light on the design of QCLs.

ACKNOWLEDGMENTS

This paper was supported by the National Natural Science Foundation of China under Grants No. 12393831, No. 11925407, and No. 61927901, the Key Research Program of Frontier Sciences, Chinese Academy of Sciences (CAS) under Grants No. ZDBS-LY-JSC019, CAS Project for Young Scientists in Basic Research under Grant No. YSBR-026, and the Strategic Priority Research Program of the CAS under Grant No. XDB43020000.

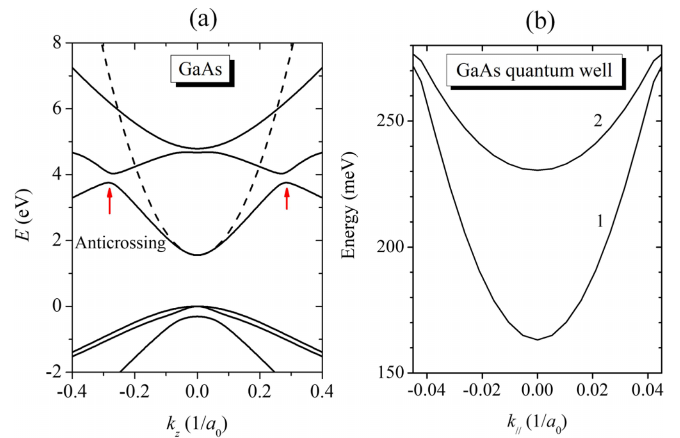

FIG. 5. (a) Band structure of bulk GaAs. The dotted and solid lines denote the dispersion of effective mass-approximated parabolic simulation and atomic pseudopotential simulation. Red arrows point to band anticrossings. (b) The in-plane energy dispersion of the conduction subbands for a GaAs/AlAs quantum well with a 4-nm-thick well.

APPENDIX: NONPARABOLIC IN-PLANE DISPERSIONS IN QWS

In this appendix, we seek to figure out how to restrain the broadening due to the nonparabolic dispersion relationship of the lasing subbands. Figure 5 shows the band structure of bulk GaAs and in-plane energy dispersions of the conduction subbands for a GaAs/AlAs QW with a 4-nm-thick well.

The nonparabolicity of the lowest conduction band induced by the $\mathbf{k}\cdot\mathbf{p}$ coupling with other bands becomes particularly strong for narrow-gap semiconductors [89]. In the effective mass approximations, an energy-dependent mass is used to consider the effect of the nonparabolicity on energy levels in finite gap semiconductors. In the context of QCLs, the one-band effective mass approximation models [21,76] are exclusively employed to describe the electronic structure, in which an energy-dependent mass is used to correct the energy levels of subbands. However, the deviation from the parabolic energy dispersion gives rise to nonparabolicity, which occurs even in the simplest band of the lowest conduction band near the Γ point in semiconductors. However, the nonparabolicity is frequently ignored in subbands, between which the electrons transition to emitting photons. Specifically, the nonparabolicity of the conduction subbands becomes important as the in-plane wave vector gets far away from the zone center or the Γ point, resulting from high carrier concentration or high temperature. The nonparabolicity of subbands has been examined to broaden the transition as $\Delta E = E_F \frac{E_{21}}{E_G}$ according to the effective mass approximation (where E_F is the Fermi level, E_{21} the band edge separation between subbands 1 and 2, and E_G the bulk band gap of the well material). Considering

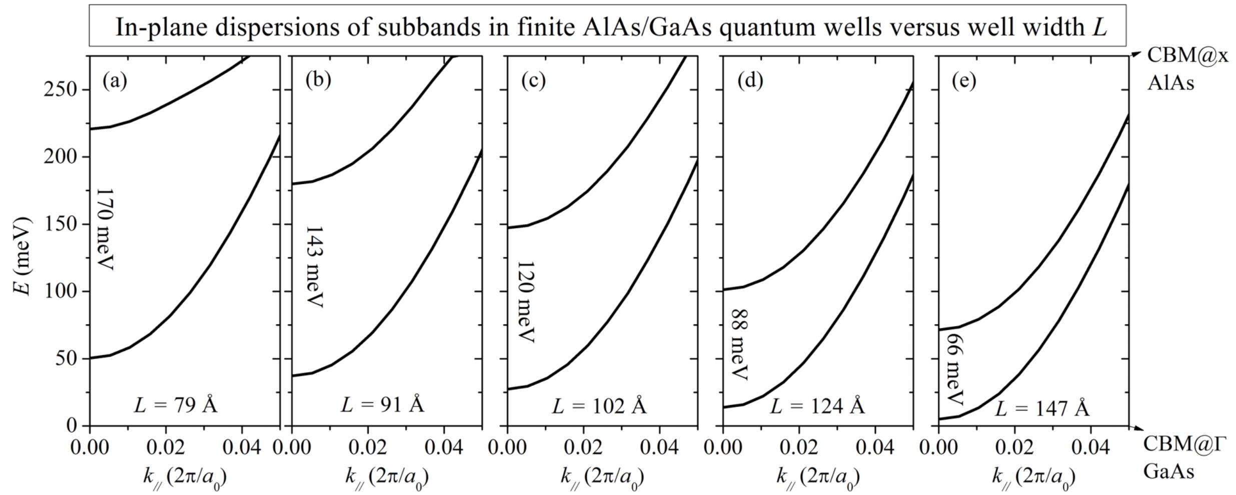

FIG. 6. Dispersion relationship of subbands along (1, 0) direction in k_xk_y plane in AlAs/GaAs quantum well with well widths $L = 79$, 91, 102, 124, and 147 Å.

the nonparabolicity of subbands, an overestimated linewidth of 20 meV was predicted in comparison with an experimentally measured linewidth of 6.6 meV [77] for an InAs/AlSb QW doped to a sheet electron density of 10^{12} cm^{-2}. It was subsequently argued [77] that the depolarization effect [78] remarkably narrows the absorption peak due to the screening of the incident field by a high-density electron gas. Since then, the band nonparabolicity has been completely excluded as a potential factor broadening the intersubband transitions in QCLs [2]. However, there is renewed interest in the impact of band nonparabolicity on the optical and transport properties of semiconductors [79–82] and the properties of thermoelectric materials [83,84]. We also note that Załużny [78] has demonstrated that the depolarization effect depends sensitively on the electron density and is negligible for a low density of $N_s = 1 \times 10^{11}$ cm^{-2}, which is on the order of electron densities in the upper lasing subband for operating QCLs [32,85,86]. By considering the nonparabolicity, authors of a very recent study illustrated that the IFR scattering contributes to only ∼50% of the optical linewidth for a QCL emitting at ∼5 μm wavelength [26]. Furthermore, linewidth broadening induced by optical transitions rather than two lasing subbands has been observed experimentally in state-of-the-art QCLs with the bound-to-continuum design [21].

Figure 6 shows the atomistic calculation results of the in-plane energy dispersions of the ground and first excited conduction subbands in finite GaAs/AlAs QWs with well widths varying from 79 to 14.7 Å. In all QWs, the excited conduction subbands have energy dispersions that are flatter than those of the ground subband, giving rise to a heavier effective mass. This nonparallel dispersion of two subbands is a manifestation of the nonparabolicity in their parent bulk band (here is the lowest conduction band of bulk GaAs), which is described by an energy-dependent effective mass in $\mathbf{k} \cdot \mathbf{p}$ approximation. The deviation of two subbands from parallel dispersions gets larger with increasing energy separation, which results from the stronger confinement in the narrower QW. It indicates that, in addition to the nonparabolicity of the parent bulk band, there is another factor that contributes to the nonparallel dispersion of two subbands. As the energy of the excited subband approaches the barrier energy to be less confined inside the well, the band dispersion will get flat. The nonparallel dispersion of two transition subbands not only arises from the nonparabolicity of the parent bulk band but also from the electronic delocalization due to the finite barrier height. It demonstrates that a wider QW is preferred to reduce the linewidth broadening caused by the nonparallel dispersion of the two lasing subbands in QCLs.

[1] J. Faist, F. Capasso, D. L. Sivco, C. Sirtori, A. L. Hutchinson, and A. Y. Cho, Quantum cascade laser, Science **264**, 553 (1994).

[2] J. Faist, *Quantum Cascade Lasers* (Oxford University Press, Oxford, 2013).

[3] S. L. Chuang, *Physics of Photonic Devices* (Wiley, Hoboken, 2009).

[4] R. Köhler, A. Tredicucci, F. Beltram, H. E. Beere, E. H. Linfield, A. G. Davies, D. A. Ritchie, R. C. Iotti, and F. Rossi, Terahertz semiconductor-heterostructure laser, Nature (London) **417**, 156 (2002).

[5] M. Razeghi, W. Zhou, S. Slivken, Q.-Y. Lu, D. Wu, and R. McClintock, Recent progress of quantum cascade laser research from 3 to 12 μm at the Center for Quantum Devices [Invited], Appl. Opt. **56**, H30 (2017).

[6] N. Zhuo, F. Liu, and Z. Wang, Quantum cascade lasers: From sketch to mainstream in the mid and far infrared, J. Semicond. **41**, 010301 (2020).

[7] N. Bandyopadhyay, Y. Bai, S. Tsao, S. Nida, S. Slivken, and M. Razeghi, Room temperature continuous wave operation of λ ∼ 3–3.2 μm quantum cascade lasers, Appl. Phys. Lett. **101**, 241110 (2012).

[8] M. Razeghi, Q. Y. Lu, N. Bandyopadhyay, W. Zhou, D. Heydari, Y. Bai, and S. Slivken, Quantum cascade lasers: From tool to product, Opt. Express **23**, 8462 (2015).

[9] Y. Bai, N. Bandyopadhyay, S. Tsao, S. Slivken, and M. Razeghi, Room temperature quantum cascade lasers with 27% wall plug efficiency, Appl. Phys. Lett. **98**, 181102 (2011).
[10] C. A. Curwen, J. L. Reno, and B. S. Williams, Terahertz quantum cascade VECSEL with watt-level output power, Appl. Phys. Lett. **113**, 011104 (2018).
[11] Y. Jin, J. L. Reno, and S. Kumar, Phase-locked terahertz plasmonic laser array with 2 W output power in a single spectral mode, Optica **7**, 708 (2020).
[12] A. Khalatpour, A. K. Paulsen, C. Deimert, Z. R. Wasilewski, and Q. Hu, High-power portable terahertz laser systems, Nat. Photonics **15**, 16 (2020).
[13] M. S. Vitiello and A. Tredicucci, Physics and technology of terahertz quantum cascade lasers, Adv. Phys. X **6**, 1893809 (2021).
[14] T. Fei, S. Q. Zhai, J. C. Zhang, N. Zhuo, J. Q. Liu, L. J. Wang, S. M. Liu, Z. W. Jia, K. Li, Y. Q. Sun *et al.*, High power $\lambda \sim 8.5$ μm quantum cascade laser grown by MOCVD operating continuous-wave up to 408 K, J. Semicond. **42**, 112301 (2021).
[15] J. Faist, C. Sirtori, F. Capasso, L. Pfeiffer, and K. W. West, Phonon limited intersubband lifetimes and linewidths in a two-dimensional electron gas, Appl. Phys. Lett. **64**, 872 (1994).
[16] C. Sirtori, Terahertz race heats up, Nat. Photonics **15**, 1 (2020).
[17] A. Wittmann, T. Gresch, E. Gini, L. Hvozdara, N. Hoyler, M. Giovannini, and J. Faist, High-performance bound-to-continuum quantum-cascade lasers for broad-gain applications, IEEE J. Quantum Electron. **44**, 36 (2008).
[18] P. Q. Liu, A. J. Hoffman, M. D. Escarra, K. J. Franz, J. B. Khurgin, Y. Dikmelik, X. Wang, J.-Y. Fan, and C. F. Gmachl, Highly power-efficient quantum cascade lasers, Nat. Photon. **4**, 95 (2010).
[19] T. Unuma, T. Takahashi, T. Noda, M. Yoshita, H. Sakaki, M. Baba, and H. Akiyama, Effects of interface roughness and phonon scattering on intersubband absorption linewidth in a GaAs quantum well, Appl. Phys. Lett. **78**, 3448 (2001).
[20] T. Unuma, M. Yoshita, T. Noda, H. Sakaki, and H. Akiyama, Intersubband absorption linewidth in GaAs quantum wells due to scattering by interface roughness, phonons, alloy disorder, and impurities, J. Appl. Phys. **93**, 1586 (2003).
[21] A. Wittmann, Y. Bonetti, J. Faist, E. Gini, and M. Giovannini, Intersubband linewidths in quantum cascade laser designs, Appl. Phys. Lett. **93**, 141103 (2008).
[22] S. Tsujino, A. Borak, E. Müller, M. Scheinert, C. V. Falub, H. Sigg, D. Grützmacher, M. Giovannini, and J. Faist, Interface-roughness-induced broadening of intersubband electroluminescence in *p*-SiGe and *n*-GaInAs/AlInAs quantum-cascade structures, Appl. Phys. Lett. **86**, 062113 (2005).
[23] J. Y. Cheng, P. Quach, D. Wang, F. Liu, S. F. Liu, L. Y. Yang, H. P. Liu, B. Shen, Y. Z. Tong, and X. Q. Wang, Dominant influence of interface roughness scattering on the performance of GaN terahertz quantum cascade lasers, Nanoscale Res. Lett. **14**, 206 (2019).
[24] Y. Chiu, Y. Dikmelik, P. Q. Liu, N. L. Aung, J. B. Khurgin, and C. F. Gmachl, Importance of interface roughness induced intersubband scattering in mid-infrared quantum cascade lasers, Appl. Phys. Lett. **101**, 171117 (2012).
[25] M. Virgilio, D. Sabbagh, M. Ortolani, L. Di Gaspare, G. Capellini, and M. De Seta, Physical mechanisms of intersubband-absorption linewidth broadening ins-Ge/SiGe quantum wells, Phys. Rev. B **90**, 155420 (2014).
[26] A. Kolek, G. Hałdaś, P. Gutowski, G. Sobczak, D. Pierścińska, and M. Bugajski, Linewidth broadening in short-wavelength quantum cascade lasers, Phys. Rev. Appl. **17**, 014019 (2022).
[27] T. Kotani, M. Arita, and Y. Arakawa, Doping dependent blue shift and linewidth broadening of intersubband absorption in non-polar *m*-plane AlGaN/GaN multiple quantum wells, Appl. Phys. Lett. **107**, 112107 (2015).
[28] Y. V. Flores and A. Albo, Impact of interface roughness scattering on the performance of $GaAs/Al_xGa_{1-x}As$ terahertz quantum cascade lasers, IEEE J. Quantum Electron. **53**, 2300208 (2017).
[29] M. Franckié, D. O. Winge, J. Wolf, V. Liverini, E. Dupont, V. Trinité, J. Faist, and A. Wacker, Impact of interface roughness distributions on the operation of quantum cascade lasers, Opt. Express **23**, 5201 (2015).
[30] E. Paysen, S. Schütt, S. Michler, Q. Yang, R. Aidam, and A. Trampert, Interface tomography of GaInAs/AlInAs quantum cascade laser active regions, Semicond. Sci. Technol. **38**, 055009 (2023).
[31] L. J. Mawst and D. Botez, High-power mid-infrared ($\lambda \sim 3$–6 μm) quantum cascade laser, IEEE Photonics J. **14**, 1508025 (2022).
[32] C. A. Wang, B. Schwarz, D. F. Siriani, I. E. E. E. Member, L. J. Missaggia, M. K. Connors, T. S. Mansuripur, D. R. Calawa, D. McNulty, M. Nickerson *et al.*, MOVPE growth of LWIR AlInAs/GaInAs/InP quantum cascade lasers: Impact of growth and material quality on laser performance, IEEE J. Sel. Top. Quantum Electron. **23**, 1200413 (2017).
[33] T. Grange, S. Mukherjee, G. Capellini, M. Montanari, L. Persichetti, L. Di Gaspare, S. Birner, A. Attiaoui, O. Moutanabbir, M. Virgilio *et al.*, Atomic-scale insights into semiconductor heterostructures: From experimental three-dimensional analysis of the interface to a generalized theory of interfacial roughness scattering, Phys. Rev. Appl. **13**, 044062 (2020).
[34] S. Mathonnière, M. P. Semtsiv, and W. T. Masselink, Thermal annealing of lattice-matched InGaAs/InAlAs quantum-cascade lasers, J. Cryst. Growth **477**, 258 (2017).
[35] A. Y. Song, R. Bhat, P. Bouzi, C.-E. Zah, and C. F. Gmachl, Three-dimensional interface roughness in layered semiconductor structures and its effect on intersubband transitions, Phys. Rev. B **94**, 165307 (2016).
[36] N. Tran, G. Biasiol, A. Jollivet, A. Bertocci, F. Julien, J.-M. Manceau, and R. Colombelli, Evidence of intersubband linewidth narrowing using growth interruption technique, Photonics **6**, 38 (2019).
[37] F.-Q. Liu, L. Li, L. Wang, J. Liu, W. Zhang, Q. Zhang, W. Liu, Q. Lu, and Z. Wang, Solid source MBE growth of quantum cascade lasers, Appl. Phys. A **97**, 527 (2009).
[38] L. Diehl, S. Menteşe, E. Müller, D. Grützmacher, H. Sigg, U. Gennser, I. Sagnes, Y. Campidelli, O. Kermarrec, D. Bensahel *et al.*, Electroluminescence from strain-compensated $Si_{0.2}Ge_{0.8}/Si$ quantum-cascade structures based on a bound-to-continuum transition, Appl. Phys. Lett. **81**, 4700 (2002).
[39] J. Faist, D. Hofstetter, M. Beck, T. Aellen, M. Rochat, and S. Blaser, Bound-to-continuum and two-phonon resonance quantum-cascade lasers for high duty cycle, high-temperature operation, IEEE J. Quantum Electron. **38**, 533 (2002).
[40] L. Bosco, M. Franckié, G. Scalari, M. Beck, A. Wacker, and J. Faist, Thermoelectrically cooled THz quantum cascade laser operating up to 210 K, Appl. Phys. Lett. **115**, 010601 (2019).

[41] M. Franckié, L. Bosco, M. Beck, C. Bonzon, E. Mavrona, G. Scalari, A. Wacker, and J. Faist, Two-well quantum cascade laser optimization by non-equilibrium Green's function modelling, Appl. Phys. Lett. **112**, 021104 (2018).
[42] L.-W. Wang and A. Zunger, Local-density-derived semiempirical pseudopotentials, Phys. Rev. B **51**, 17398 (1995).
[43] J.-W. Luo, G. Bester, and A. Zunger, Atomistic pseudopotential calculations of thickness-fluctuation GaAs quantum dots, Phys. Rev. B **79**, 125329 (2009).
[44] J.-W. Luo and A. Zunger, Geometry of epitaxial GaAs/(Al, Ga)As quantum dots as seen by excitonic spectroscopy, Phys. Rev. B **84**, 235317 (2011).
[45] D. M. Wood and A. Zunger, Successes and failures of the **k**·**p** method: A direct assessment for GaAs/AlAs quantum structures, Phys. Rev. B **53**, 7949 (1996).
[46] I. Saïdi, S. Ben Radhia, and K. Boujdaria, Band parameters of GaAs, InAs, InP, and InSb in the 40-band **k**·**p** model, J. Appl. Phys. **107**, 043701 (2010).
[47] R. Neffati, I. Saïdi, and K. Boujdaria, Full-zone **k**·**p** model for the electronic structure of unstrained $GaAs_{1-x}P_x$ and strained $Al_xIn_{1-x}As$ alloys, J. Appl. Phys. **112**, 053716 (2012).
[48] G. Bastard, Superlattice band structure in the envelope-function approximation, Phys. Rev. B **24**, 5693 (1981).
[49] G. Bastard, Theoretical investigations of superlattice band structure in the envelope-function approximation, Phys. Rev. B **25**, 7584 (1982).
[50] G. Bastard, *Wave Mechanics Applied to Semiconductor Heterostructures* (Les Editions de Physiques, Paris, 1992).
[51] J.-M. Jancu, R. Scholz, F. Beltram, and F. Bassani, Empirical spds* tight-binding calculation for cubic semiconductors: General method and material parameters, Phys. Rev. B **57**, 6493 (1998).
[52] C. Jirauschek and T. Kubis, Modeling techniques for quantum cascade lasers, Appl. Phys. Rev. **1**, 011307 (2014).
[53] J.-W. Luo, A. N. Chantis, M. van Schilfgaarde, G. Bester, and A. Zunger, Discovery of a novel linear-in-*k* spin splitting for holes in the 2D GaAs/AlAs system, Phys. Rev. Lett. **104**, 066405 (2010).
[54] J.-W. Luo, G. Bester, and A. Zunger, Supercoupling between heavy-hole and light-hole states in nanostructures, Phys. Rev. B **92**, 165301 (2015).
[55] J.-W. Luo, S.-S. Li, and A. Zunger, Rapid transition of the hole Rashba effect from strong field dependence to saturation in semiconductor nanowires, Phys. Rev. Lett. **119**, 126401 (2017).
[56] J.-X. Xiong, S. Guan, J.-W. Luo, and S.-S. Li, Emergence of strong tunable linear Rashba spin-orbit coupling in two-dimensional hole gases in semiconductor quantum wells, Phys. Rev. B **103**, 085309 (2021).
[57] C. Pryor, J. Kim, L. W. Wang, A. J. Williamson, and A. Zunger, Comparison of two methods for describing the strain profiles in quantum dots, J. Appl. Phys. **83**, 2548 (1998).
[58] K. Kim, P. R. C. Kent, A. Zunger, and C. B. Geller, Atomistic description of the electronic structure of $In_xGa_{1-x}As$ alloys and InAs/GaAs superlattices, Phys. Rev. B **66**, 045208 (2002).
[59] K. A. Mader and A. Zunger, Empirical atomic pseudopotentials for AlAs/GaAs superlattices, alloys, and nanostructures, Phys. Rev. B **50**, 17393 (1994).
[60] J.-W. Luo, P. Stradins, and A. Zunger, Matrix-embedded silicon quantum dots for photovoltaic applications: A theoretical study of critical factors, Energy Environ. Sci. **4**, 2546 (2011).
[61] L. W. Wang and A. Zunger, Solving Schrödinger's equation around a desired energy: Application to silicon quantum dots, J. Chem. Phys. **100**, 2394 (1994).
[62] A. Franceschetti and A. Zunger, The inverse band-structure problem of finding an atomic configuration with given electronic properties, Nature (London) **402**, 60 (1999).
[63] L. Zhang, J. W. Luo, A. Saraiva, B. Koiller, and A. Zunger, Genetic design of enhanced valley splitting towards a spin qubit in silicon, Nat. Commun. **4**, 2396 (2013).
[64] M. d'Avezac, J. W. Luo, T. Chanier, and A. Zunger, Genetic-algorithm discovery of a direct-gap and optically allowed superstructure from indirect-gap Si and Ge semiconductors, Phys. Rev. Lett. **108**, 027401 (2012).
[65] L.-W. Wang, J. Kim, and A. Zunger, Electronic structures of [110]-faceted self-assembled pyramidal InAs/GaAs quantum dots, Phys. Rev. B **59**, 5678 (1999).
[66] M. Ediger, G. Bester, A. Badolato, P. M. Petroff, K. Karrai, A. Zunger, and R. J. Warburton, Peculiar many-body effects revealed in the spectroscopy of highly charged quantum dots, Nat. Phys. **3**, 774 (2007).
[67] J.-W. Luo, R. Singh, A. Zunger, and G. Bester, Influence of the atomic-scale structure on the exciton fine-structure splitting in InGaAs and GaAs quantum dots in a vertical electric field, Phys. Rev. B **86**, 161302(R) (2012).
[68] L. Zhang, M. d'Avezac, J. W. Luo, and A. Zunger, Genomic design of strong direct-gap optical transition in Si/Ge core/multishell nanowires, Nano Lett. **12**, 984 (2012).
[69] A. Lyakh, R. Maulini, A. Tsekoun, R. Go, C. Pflügl, L. Diehl, Q. J. Wang, F. Capasso, and C. K. N. Patel, 3 W continuous-wave room temperature single-facet emission from quantum cascade lasers based on nonresonant extraction design approach, Appl. Phys. Lett. **95**, 141113 (2009).
[70] L. Li, L. Chen, J. Zhu, J. Freeman, P. Dean, A. Valavanis, A. G. Davies, and E. H. Linfield, Terahertz quantum cascade lasers with >1 W output powers, Electron. Lett. **50**, 309 (2014).
[71] M. A. Belkin and F. Capasso, New frontiers in quantum cascade lasers: High performance room temperature terahertz sources, Phys. Scr. **90**, 118002 (2015).
[72] A. M. Andrews, T. Zederbauer, H. Detz, D. MacFarland, W. Schrenk, and G. Strasser, Chapter 26—THz quantum cascade lasers, in *Molecular Beam Epitaxy (Second Edition): From Research to Mass Production*, edited by M. Henini (Elsevier, Waltham, 2018) pp. 597.
[73] V. Rindert, E. Önder, and A. Wacker, Analysis of high-performing terahertz quantum cascade lasers, Phys. Rev. Appl. **18**, L041001 (2022).
[74] J. C. Portal and G. Gregoris, Two-dimensional magnetophonon resonance in GaInAs-InP and GaInAs-AlInAs heterojunctions and superlattice, Surf. Sci. **142**, 368 (1984).
[75] M. A. Brummell, R. J. Nicholas, J. C. Portal, K. Y. Cheng, and A. Y. Cho, Two-dimensional magnetophonon resonance. II. GaInAs-AlInAs heterojunctions, J. Phys. C: Solid State Phys. **16**, L579 (1983).
[76] C. Sirtori, F. Capasso, J. Faist, and S. Scandolo, Nonparabolicity and a sum rule associated with bound-to-bound and bound-to-continuum intersubband transitions in quantum wells, Phys. Rev. B **50**, 8663 (1994).

[77] R. J. Warburton, C. Gauer, A. Wixforth, J. P. Kotthaus, B. Brar, and H. Kroemer, Intersubband resonances in InAs/AlSb quantum wells: Selection rules, matrix elements, and the depolarization field, Phys. Rev. B **53**, 7903 (1996).

[78] M. Załużny, Intersubband absorption line broadening in semiconductor quantum wells: Nonparabolicity contribution, Phys. Rev. B **43**, 4511 (1991).

[79] N. Preissler, O. Bierwagen, A. T. Ramu, and J. S. Speck, Electrical transport, electrothermal transport, and effective electron mass in single-crystalline In_2O_3 films, Phys. Rev. B **88**, 085305 (2013).

[80] K. Krishnaswamy, B. Himmetoglu, Y. Kang, A. Janotti, and C. G. Van de Walle, First-principles analysis of electron transport in $BaSnO_3$, Phys. Rev. B **95**, 205202 (2017).

[81] Y. Kang and S. Han, Intrinsic carrier mobility of cesium lead halide perovskites, Phys. Rev. Appl. **10**, 044013 (2018).

[82] L. D. Whalley, J. M. Frost, B. J. Morgan, and A. Walsh, Impact of nonparabolic electronic band structure on the optical and transport properties of photovoltaic materials, Phys. Rev. B **99**, 085207 (2019).

[83] N. A. Mecholsky, L. Resca, I. L. Pegg, and M. Fornari, Theory of band warping and its effects on thermoelectronic transport properties, Phys. Rev. B **89**, 155131 (2014).

[84] Z. M. Gibbs, F. Ricci, G. Li, H. Zhu, K. Persson, G. Ceder, G. Hautier, A. Jain, and G. J. Snyder, Effective mass and Fermi surface complexity factor from *ab initio* band structure calculations, npj Comput. Mater. **3**, 8 (2017).

[85] J. Faist, F. Capasso, C. Sirtori, D. L. Sivco, A. L. Hutchinson, and A. Y. Cho, Room temperature mid-infrared quantum cascade lasers, Electron. Lett **32**, 560 (1996).

[86] C. Gmachl, F. Capasso, D. L. Sivco, and A. Y. Cho, Recent progress in quantum cascade lasers and applications, Rep. Prog. Phys. **64**, 1533 (2001).

[87] A. Leuliet, A. Vasanelli, A. Wade, G. Fedorov, D. Smirnov, G. Bastard, and C. Sirtori, Electron scattering spectroscopy by a high magnetic field in quantum cascade lasers, Phys. Rev. B **73**, 085311 (2006).

[88] T. Kubis, C. Yeh, and P. Vogl, Quantum theory of transport and optical gain in quantum cascade lasers, Phys. Status Solidi C **5**, 232 (2008).

[89] E. O. Kane, Band structure of indium antimonide, J. Phys. Chem. Solids **1**, 249 (1957).